Supplemental Material

Tunable Atomically Enhanced Moiré Berry Curvatures in Twisted Triple Bilayer Graphene

Konstantin Davydov[1], Ziyan Zhu[2], Noah Friedman[1], Ethan Gramowski[1], Yaotian Li[1], Jack Tavakley[1], Kenji Watanabe[3], Takashi Taniguchi[4], Mitchell Luskin[5], Efthimios Kaxiras[6,7], Ke Wang[1*]

[1]*School of Physics and Astronomy, University of Minnesota, Minneapolis, Minnesota 55455, USA*
[2]*Stanford Institute for Materials and Energy Sciences, SLAC National Accelerator Laboratory, Menlo Park, CA 94025, USA*
[3] *Research Center for Electronic and Optical Materials, National Institute for Materials Science, 1-1 Namiki, Tsukuba 305-0044, Japan*
[4] *Research Center for Materials Nanoarchitectonics, National Institute for Materials Science, 1-1 Namiki, Tsukuba 305-0044, Japan*
[5]*School of Mathematics, University of Minnesota, Minneapolis, Minnesota 55455, USA*
[6]*Department of Physics, Harvard University, Cambridge, Massachusetts 02138, USA*
[7]*John A. Paulson School of Engineering and Applied Sciences, Harvard University, Cambridge, Massachusetts 02138*
**Corresponding author. Email: kewang@umn.edu*

S1. Sample preparation, device fabrication, and electrical transport measurements

The dual-gated twisted triple bilayer graphene (tTBLG) stack was made using the "cut and stack" method [1]. A single bilayer graphene (BLG) flake was cut into three individual pieces with the same lattice orientation using the cantilever of an XE7 atomic force microscope (AFM) from Park Systems. Using a poly (bisphenol A carbonate) (PC) and polydimethylsiloxane (PDMS) stamp mounted on a glass slide, a top hexagonal boron nitride [2] (hBN) flake, few layer graphite (serving as the top gate) and middle hBN (isolating the graphite gate from tTBLG) were picked up. Next, the three precut pieces of BLG were successively picked up. After each pick up step, the remaining pieces of BLG were rotated at angles of 1.49° and 1.68° in the same direction. Finally, the tTBLG was encapsulated by picking up a bottom hBN, and the complete stack was released onto a SiO_2(285 nm)/Si substrate at 180℃. The PC residue on top of the stack was cleaned by sequentially rinsing the chip containing the stack in chloroform, acetone and isopropanol. Afterwards, a bubble free area of the device serving as the active region was found using the AFM, ensuring the high quality of the device. Ohmic contacts [3] to 1D boundaries of the tTBLG were then added using electron-beam lithography, dry etching, and subsequent metal deposition (Cr/Pd/Au, 1 nm /5 nm/>180 nm). Finally, the active region was given a Hall bar shape [Fig. 1(b)] by a round of electron-beam lithography and reactive ion dry etching.

The electrical and magneto-transport measurements were performed in a Bluefors LD250 cryostat at base temperature of $T = 10$ mK and temperatures ranging from 10 mK to 20 K (for T-dependence) with magnetic fields up to 8 T. The four-probe measurements of the device were performed with 0.5, 1, 10, and 200 nA AC current excitations at a frequency of 17.777 Hz. The voltage drops across the device were measured with the help of SR830 lock-in amplifiers (Stanford Research Systems). The top and back gate voltages were controlled by two voltage sources (Yokogawa: Model GS200 and Keithley Instruments: Model 2400 respectively).

S2. Calculation of displacement field and charge carrier density from top and bottom gate capacitive coupling

The displacement field, D, between the graphite top and silicon back gates and the charge carrier density, n, are both calculated by estimating the capacitive coupling of each gate to tTBLG. By using a parallel-plate capacitor model, we find $D = (-C_{TG}V_{TG} + C_{BG}V_{BG})/2 + D_0$, $n = (C_{TG}V_{TG} + C_{BG}V_{BG})/e + n_0$, where $V_{TG}(V_{BG})$ are top (back) gate voltages, $C_{TG}(C_{BG})$ are the top(back) gate capacitances per unit area, D_0, n_0 are the displacement field and charge carrier offsets, e is the elementary charge. The capacitance of the top gate is given by $C_{TG} = \varepsilon_{hBN}/d_t$, where $\varepsilon_{hBN} = 3.76\varepsilon_0$ is the hBN permittivity, ε_0 is the vacuum permittivity, and $d_t = 23$ nm is the hBN thickness separating the top gate from tTBLG. The back gate has the effective capacitance of two capacitors (with separations due to SiO_2 and bottom hBN dielectrics) in series found from $1/C_{BG} = 1/C_{SiO_2} + 1/C_b$, where $C_{SiO_2} = \varepsilon_{SiO_2}/d_{SiO2}$ and $C_b = \varepsilon_{hBN}/d_b$ with $\varepsilon_{SiO_2} = 3.9\varepsilon_0$ being the SiO_2 permittivity, $d_{SiO_2} = 285$ nm and $d_b = 44$ nm being the SiO_2 and bottom hBN thicknesses respectively. The finite offsets, D_0, n_0, can be explained by Schottky barriers at the layer interfaces or slight intrinsic doping in tTBLG. The size of $n_0 \sim 1\times10^{11}$ cm^{-2} is characterized by the gate voltage needed to compensate for the offset of the charge neutrality peak from the zero voltage. Same voltage gives D_0/ε_0 of the order of ~ 0.01V/nm.

S3. Valley Hall effect from additional band insulator states

The valley Hall effect can be observed at multiple BI states in the tTBLG device. In addition to the $\nu_T = -4$ and MoM BI states, Berry curvature hot spots are present near the $\nu_T = 4$ and $\nu_B = 4$ fillings [Fig. 2(b)]. At both fillings, nonlocal measurements following the protocol from the main manuscript demonstrate a nonlocal resistance more than one order of magnitude larger than trivial Ohmic contribution due to stray currents [Figs. S1(a) and S1(b)]. Figures S1(c) and S1(d) show the nonlocal resistance, R_{NL}, as a function of the local one R_L near the $\nu_T = 4$ and $\nu_B = 4$ fillings respectively. The plotted resistance dependence shows a clear difference between the hole-like (red) and electron-like (blue) carriers changing the type across the BI state. The nonlocal resistance for each carrier type follows a nonlinear power law relationship $R_{NL} \sim R_L^{\gamma}$ with the power $\gamma = \gamma_h$ (γ_e) extracted from separate fittings for hole- (electron-) like R_{NL}. Both powers being sufficiently different from $\gamma = 1$ at varying D [Figs. S1(e) and S1(f)] indicate a non-Ohmic mechanism of nonlocal transport through valley current due to a Berry curvature hot spot. When the ballistic valley-chiral channel is completely saturated, the power γ reaches zero. In the opposite scenario, when the valley-chiral channel is established, yet far from saturation, the power is expected to approach $\gamma \to 3$.

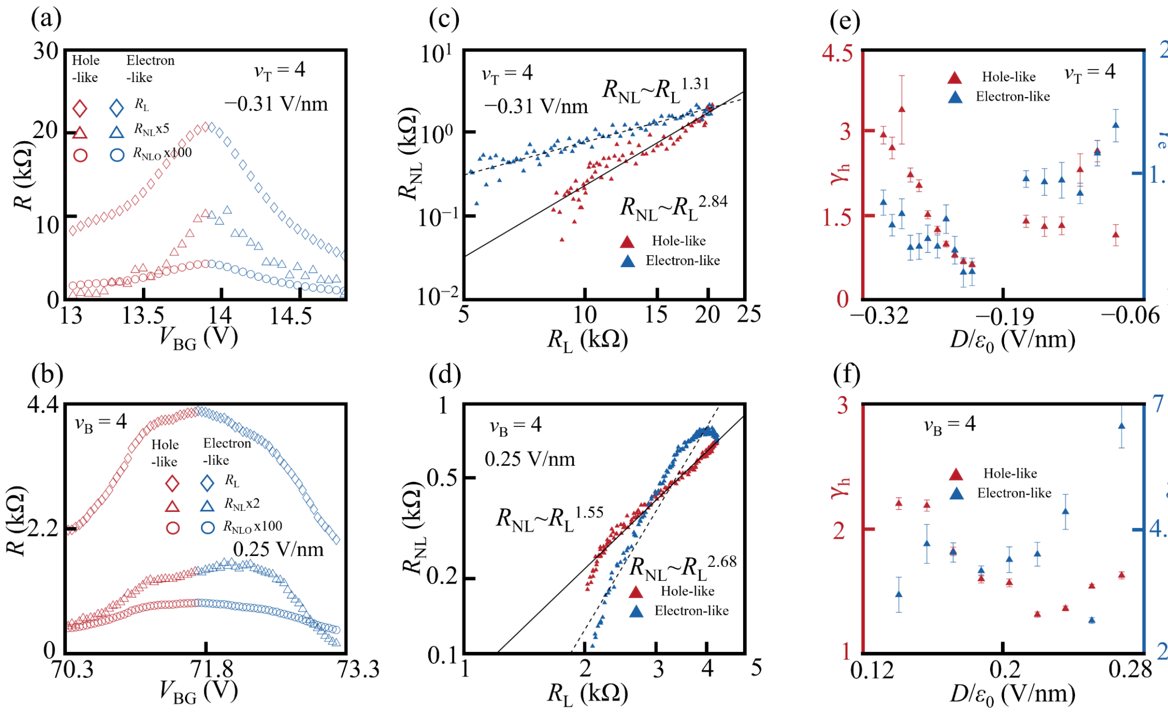

FIG. S1. Valley Hall effect at $\nu_T = 4$ and $\nu_B = 4$ in tTBLG. (a) and (b) Back gate voltage dependance of the local (R_L), nonlocal (R_{NL}) and nonlocal Ohmic resistance (R_{NLO}) near the $\nu_T = 4$ and $\nu_B = 4$ BI states at $D/\varepsilon_0 = -0.31$ V/nm and $D/\varepsilon_0 = 0.25$ V/nm respectively. The color highlights the types of carriers participating in electrical transport. (c) and (d) The dependence of R_{NL} on R_L for hole-like (red) and electron-like (blue) carriers at $\nu_T = 4$ and $\nu_B = 4$ and the same D as in (a) and (b). For each carrier type, the trendlines show a power law fit $R_{NL} \sim R_L^{\gamma}$. (e) and (f) The extracted power $\gamma = \gamma_h$ (γ_e) for hole- (electron-) like carriers as a function of displacement field at $\nu_T = 4$ and $\nu_B = 4$.

S4. Temperature dependance of band insulator states in tTBLG

By following the fitting procedure described in the main text, we extract the band and nonlocal gaps of the $\nu_T = 4$, $\nu_B = 4$ BI states from the temperature dependence of local and nonlocal resistances. Figs. S2(a) and S2(b) summarize the sizes of the band insulator gaps (Δ_L, diamonds) as a function of displacement field D comparing them with the nonlocal gaps (Δ_{NL}, triangles) found from the thermal activation behavior of the nonlocal resistance R_{NL} as discussed in the main manuscript. The nonlocal gaps are consistently larger than the band insulator ones confirming the presence of a Berry curvature hot spot near the band edges. As the temperature increases, the charge carriers are thermally excited between the conduction and valence bands which results in diminishing R_L. However, the larger Δ_{NL} compared to Δ_L, indicates that additional energy is needed to push the carriers away from the Berry curvature hot spot.

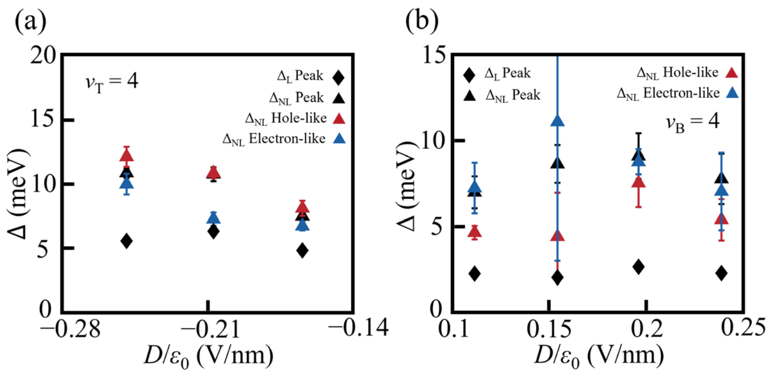

FIG. S2. Temperature dependence of the $\nu_T = 4$ and $\nu_B = 4$ band insulator states in tTBLG. (a) and (b) Displacement field dependence of band insulator Δ_L (diamonds) and nonlocal band gap Δ_{NL} (triangles) found from Arrhenius fits of the $\nu_T = 4$ and $\nu_B = 4$ BI resistance peak (black) and half peak (red and blue, with the colors corresponding to hole-like and electron-like carrier types).

S5. Results from a different region of tTBLG device

Band insulator valley Hall effect was reproduced in a different region of the same tTBLG device discussed in the main manuscript (Device 1). The main manuscript discusses the measured local resistance, R_{xx}, in Region 1 between Contact 3 and Contact 4 of the device shown in Fig. 1(b). Similarly, under the same driven current (Contact 5 serving as the source; Contacts 1, 9 serving as the drain), the four-probe longitudinal resistance, $R_L = R_{xx}$, between Contact 2 and Contact 3 corresponding to Region 2 of the same device can be measured. In this region, in addition to correlated insulator states at moiré half filling (Fig. S3), displacement field tunable band insulator states are observed at four charge carriers per top (bottom) moiré unit cell corresponding to twist angles of 1.48°±0.02° (1.66°±0.01°).

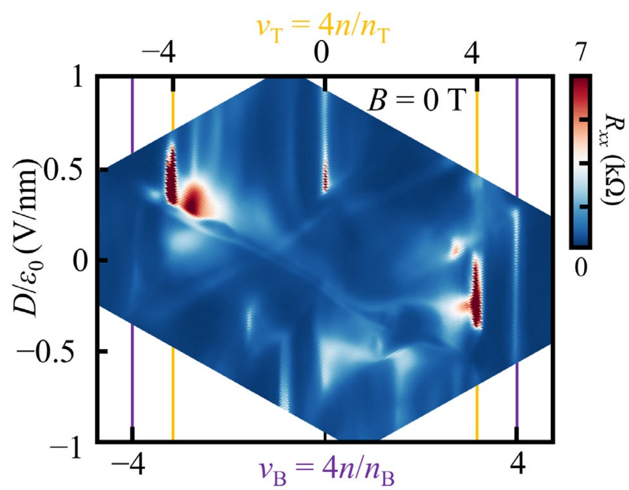

FIG. S3. Local transport in Region 2 of Device 1. Longitudinal resistance R_{xx} between Contact 2 and Contact 3 as a function of charge carrier density n and displacement field D. Resistance peaks of band insulator states (highlighted by solid lines) appearing at four charge carriers per top (yellow) and bottom (purple) moiré unit cell.

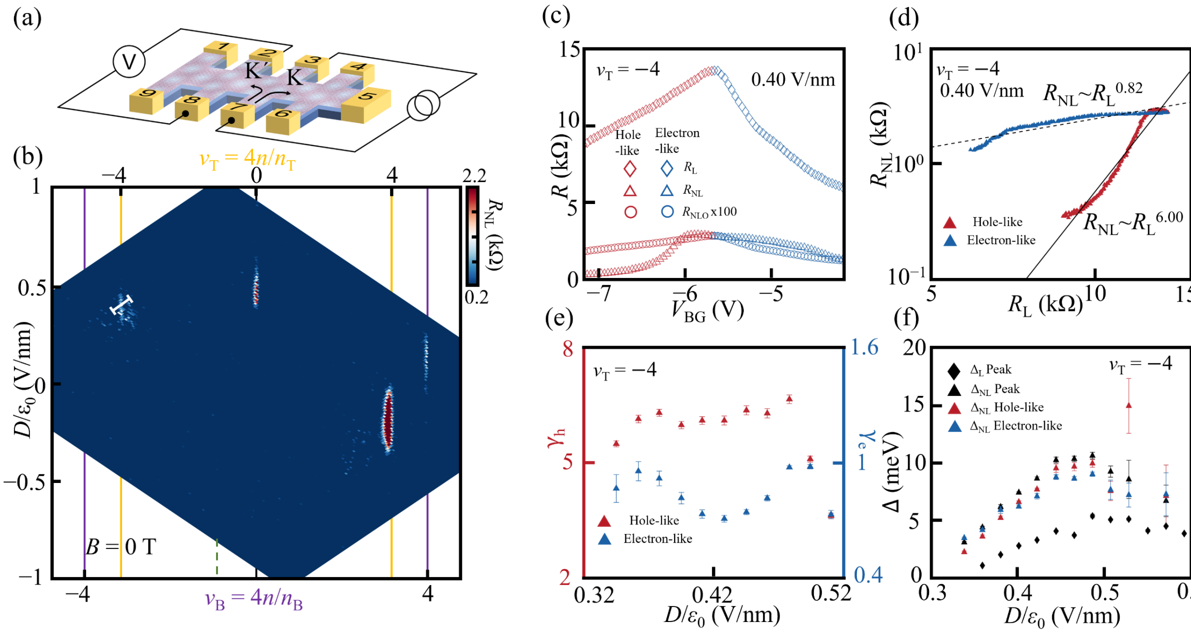

FIG. S4. Valley Hall effect in Region 2 of the tTBLG device. (a) Measurement configuration for studying nonlocal transport in Region 2 of the tTBLG device. (b) Nonlocal resistance R_{NL} = V_{82}/I_{73} found from the driven current and measured voltage in the configuration of (a) at varying D and n. The resistance peaks corresponding to the Berry curvature hot spots at ν_T = ±4, ν_B = 4 are reproduced in Region 2. The white bar represents the horizontal range in (c). (c) Nonlocal (R_{NL}), local (R_L), and calculated nonlocal Ohmic resistance (R_{NLO}) contributing to nonlocal transport of the $\nu_T = -4$ BI at $D/\varepsilon_0 = +0.40$ V/nm. (d) R_{NL} as a function of R_L for hole-like (red) and electron-like (blue) carriers across the $\nu_T = -4$ BI band gap at $D/\varepsilon_0 = +0.40$ V/nm. The dependence is consistent with power law fits for the hole-like (solid line) and electron-like (dashed line) carriers. (e) Displacement field dependence of the powers extracted from the $R_{NL}{\sim}R_L^{\gamma_h}$ ($R_{NL}{\sim}R_L^{\gamma_e}$) fits for the hole- (electron-) like charge carriers. (f) Estimated from the Arrhenius fits, the local Δ_L nonlocal Δ_{NL} bandgaps at the BI peak (black) and half peak (blue and red, corresponding to the electron- and hole-like carriers) value of the resistance as a function of D.

By driving current, I_{73}, between Contact 7 and Contact 3 and measuring voltage, V_{82}, between Contact 8 and Contact 2 [Fig. 1(b) and Fig. S4(a)], a nonlocal resistance, $R_{NL} = V_{82}/I_{73}$, in Region 2 can be found as a function of D and n [Fig. S4(b)]. Similar to Region 1, a finite nonlocal resistance is measured at ν_T = ±4, ν_B = 4, indicating the presence of Berry curvature hot spots. Near ν_T = –4, the measured R_{NL} [Fig. S4(c)] is two orders of magnitude larger than the trivial Ohmic resistance from the stray charge currents. This points to the presence of a transverse valley current responsible for the increased nonlocal resistance. The plotted R_{NL} as a function of R_L [Fig. S4(d)] reveals two separate nonlinear power law dependences, R_{NL} ~R_L^{γ}, characteristic to a valley Hall effect, for the hole-like ($\gamma = \gamma_h$) and electron-like ($\gamma = \gamma_e$) charge carrier types changing across the ν_T = –4 insulator band gap. Changing D has no consistent effect on the form of the power law dependence [Fig. S4(e)]. However, over the entire range of the displacement field, both powers differ from $\gamma = 1$ excluding the possibility of trivial Ohmic transport. Found from the resistance behavior during thermal activation, the nonlocal bandgap, Δ_{NL}, turns out to be higher than Δ_L over the entire range of displacement fields at which the nonlocal signal exists [Fig. S4(f)]. This is consistent with the Berry curvature hot spot model depicted in main manuscript Fig. 4(a).

The main experimental observations of atomically enhanced Berry curvature have been reproduced in a different region of tTBLG, suggesting the robustness of the observed emergent quantum phenomena. The differences in quantitative details (i.e., the extracted power law dependence) further supports that the Berry curvature of reconstructed bands is extremely sensitive to microscopic details of reconstructed local atomic landscape, which can realistically vary with the presence of even slight twist angle inhomogeneity.

S6. Calculation of the electronic structure

To obtain the electronic structure of tTBLG, we follow the momentum-space model in [4] with modified hopping parameters. The Hamiltonian in momentum space can then be formally written as

$$H_K(\boldsymbol{q}) = \begin{bmatrix} H^1(\boldsymbol{q}) + \delta_1 \mathbb{I}_{2\times 2} & T^{12} & 0 \\ T^{12\dagger} & H^2(\boldsymbol{q}) + \delta_2 \mathbb{I}_{2\times 2} & T^{23} \\ 0 & T^{23\dagger} & H^3(\boldsymbol{q}) + \delta_3 \mathbb{I}_{2\times 2} \end{bmatrix}. \quad (S2)$$

The diagonal blocks describe the low-energy Hamiltonian of the Bernal bilayer graphene with δ_ℓ representing the onsite potential due to the applied vertical displacement field. The intralayer parameters are taken from [5]. The off-diagonal terms describe the interlayer interaction between adjacent Bernal bilayers. More explicitly, the intralayer terms in the (A_1, B_1, A_2, B_2) basis can be expressed as:

$$H^\ell(\boldsymbol{q}) = \begin{bmatrix} H_D^{\ell,t}(\boldsymbol{q}) & g^\dagger(\boldsymbol{q}) \\ g(\boldsymbol{q}) & H_D^{\ell,b}(\boldsymbol{q}) \end{bmatrix}, \quad (S3)$$

where the superscript t/b denotes the top and bottom Bernal bilayer graphene. H_D is the rotated Dirac Hamiltonian for monolayer graphene.

$$H^{\ell,t/b}(\boldsymbol{q}) = \begin{bmatrix} \Delta_{\mathrm{t}} & \hbar v_F e^{i\theta_\ell} q_+ \\ \hbar v_F e^{i\theta_\ell} q_- & \Delta_{\mathrm{b}} \end{bmatrix}, \quad (S4)$$

where $\theta_1 = \theta_{12}$, $\theta_2 = 0$, and $\theta_3 = \theta_{23}$, and $v_F = 0.8 \times 10^6$ m/s is the monolayer graphene Fermi velocity, $q_\pm = q_x \pm q_y$. The diagonal $\Delta_{\mathrm{t/b}}$ represents the on-site potential of dimer sites with respect to nondimer sites, and $\Delta_{\mathrm{t/b}} = 0.050$ eV is the neighboring layer is not vacuum and 0 otherwise. $g(\boldsymbol{k})$ is the parabolic part of the band structure:

$$g(\boldsymbol{q}) = \begin{bmatrix} \hbar v_4\, q_+ & \gamma_1 \\ \hbar v_3 q_- & \hbar v_4 k_+ \end{bmatrix}, \quad (S5)$$

where $\gamma_1 = 0.4$ eV is the hopping between dimer sites, $\gamma_3 = 0.32$ eV, $\gamma_4 = 0.044$ eV and $v_i = \frac{\sqrt{3}\gamma_i a}{2\hbar}$ where a is the monolayer graphene lattice constant.

For the interlayer coupling, we keep the nearest neighbor coupling in momentum space

$$T_{\alpha\beta}^{ij}\left(\boldsymbol{q}^{(i)}, \boldsymbol{q}^{(j)}\right) = \sum_{n=1}^{3} T_{\alpha\beta}^{\boldsymbol{q}_n^{ij}} \delta_{\boldsymbol{q}^{(i)} - \boldsymbol{q}^{(j)}, -\boldsymbol{q}_n^{ij}}, \quad (S6)$$

where $\boldsymbol{q}_1^{ij} = K_{\mathrm{L_i}} - K_{\mathrm{L_j}}$, $\boldsymbol{q}_2^{ij} = \mathcal{R}^{-1}\left(\frac{2\pi}{3}\right)\boldsymbol{q}_1^{ij}$, $\boldsymbol{q}_3^{ij} = \mathcal{R}\left(\frac{2\pi}{3}\right)\boldsymbol{q}_1^{ij}$ and $\mathcal{R}(\theta)$ is the counterclockwise rotation matrix by θ. We take into account the out-of-plane relaxation by letting $t_{AA}^{ij} = t_{BB}^{ij} = \omega_0 = 0.07$ eV and $t_{AB}^{ij} = t_{BA}^{ij} = \omega_1 = 0.11$ eV due to the strengthened interaction between AB/BA sites from relaxation.

$$T^{\boldsymbol{q}_1^{ij}} = \begin{bmatrix} \omega_0 & \omega_1 \\ \omega_1 & \omega_0 \end{bmatrix}, T^{\boldsymbol{q}_2^{ij}} = \begin{bmatrix} \omega_0 & \omega_1\bar{\phi} \\ \omega_1\phi & \omega_0 \end{bmatrix}, T^{\boldsymbol{q}_3^{ij}} = \begin{bmatrix} \omega_0 & \omega_1\phi \\ \omega_1\bar{\phi} & \omega_0 \end{bmatrix}, \quad (S7)$$

where $\phi = e^{\frac{i2\pi}{3}}$ and $\bar{\phi} = e^{-\frac{i2\pi}{3}}$.

S7. Spatial dependence of valley currents in tTBLG

By following previously-introduced approaches [6–12], we measure the nonlocal signal R_{NL} at voltage probes located at varying distance L from the applied current [Fig. S5 and Fig. 1(b)]. In this configuration, at an electric field E driving the charge current, the Berry curvature hot spot yields a non-zero transverse valley current density (valley Hall effect), $J_{\mathrm{v}} = \sigma_{xy}^{v}E$. At a band insulator state, the transverse valley Hall conductivity σ_{xy}^{v} is expected to be Me^2/h, where M is the total Berry flux of the occupied states below the Fermi energy. Subsequently, the inverse valley Hall effect is responsible for generating the nonlocal signal R_{NL} decaying with L [Fig. S5(b)]. Following the previously established methods [6,8–10], we fit the length dependence of R_{NL} at the $\nu_{\mathrm{T}} = -4$ [Fig. S5(b)] BI state with the model expression

$$R_{\mathrm{NL}} = \left(\frac{w}{2\xi}\right)\left(\sigma_{xy}^{v}\right)^2 \rho_{xx}^3 \exp\left(-L/\xi\right), \quad (S8)$$

where w is the width of the valley channel, ξ is the valley decay length, and ρ_{xx} is the longitudinal resistivity. For $\nu_{\mathrm{T}} = -4$ BI we found ξ to be 4±2 μm, a change much slower than the decay due to diffusive Ohmic transport, and consistent with the expected inter-valley scattering lengths. For the $\nu_{\mathrm{T}} = -4$ BI state, σ_{xy}^{v} is found to be ~$3e^2/h$ confirming the Berry curvature hot spot being the origin of the nonlocal signal.

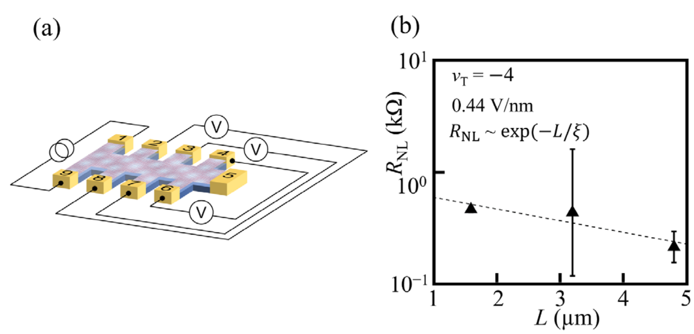

FIG. S5. Spatial dependence of valley Hall effect. (a) Nonlocal transport measurement configuration with non-local voltages simultaneously measured at different distances from the driven current. (b) R_{NL} calculated from the measured nonlocal voltages as a function of L, the distance from the driven current, at $\nu_{\mathrm{T}} = -4$ ($D/\varepsilon_0 = +0.44$ V/nm) BI state. The dashed lines represent a data fit with Equation ($S8$).

S8. Valley currents measured in additional device

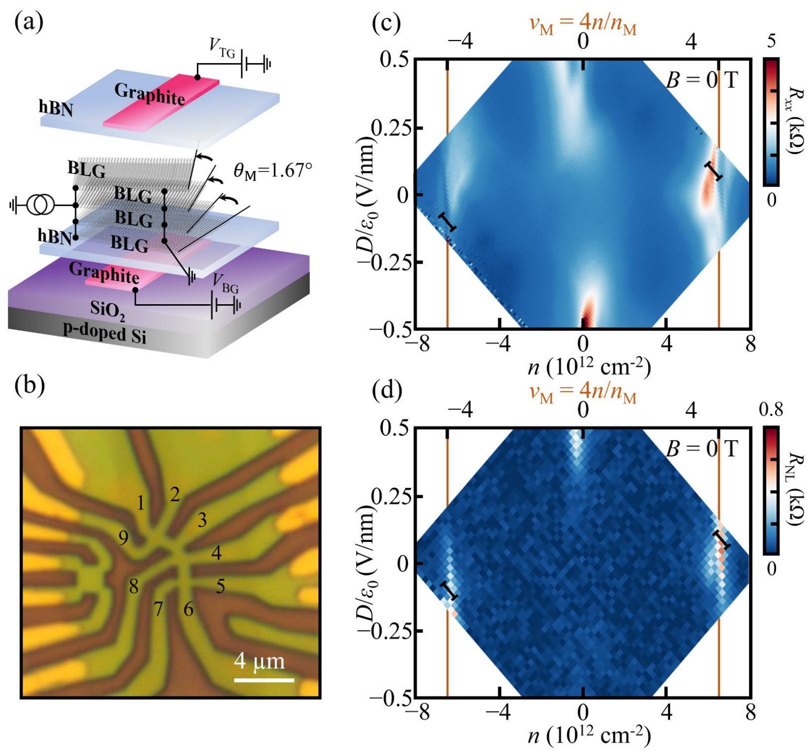

FIG. S6. Results from second device. (a) Schematic structure of the second dual gated twisted multilayer device consisting of four layers of BLG consecutively twisted in the same direction. The voltage applied to the top (V_{TG}) and bottom (V_{BG}) graphite gates controls the charge carrier density and displacement field. (b) Optical micrograph of the second device with the numbers labeling contacts to the twisted multilayer region. (c) The measured four-probe resistance R_{xx} between Contacts 4 and 5 as a function of total charge carrier density n, middle moiré filling factor ν_M and out-of-plane displacement field D. The current is driven between Contacts 1 and 6. The color plots in (c) and (d) have black bars indicating the horizontal top gate voltage ranges in Figs. S7(a) and S7(b). (d) Same as (c) but for the measured nonlocal resistance between Contacts 4 and 8 when a current is driven between Contacts 5 and 7.

Displacement field-tunable valley currents were also observed in an additional twisted multilayer system [Device 2, Figs. S6(a) and S6(b)]. The second device consists of four layers of BLG consecutively twisted with respect to each other [Fig. S6(a)]. The device was fabricated by following a similar protocol introduced in Section S1. However, an additional graphite bottom gate was picked up before the entire stack was released onto a SiO_2 substrate. The displacement field and charge carrier densities were calculated based on a parallel-place capacitor model from Section S2: $D = (-C_{TG}V_{TG} + C_{BG}V_{BG})/2 + D_0$, $n = (C_{TG}V_{TG} + C_{BG}V_{BG})/e + n_0$, where, for Device 2, $C_{TG} = \varepsilon_{hBN}/d_t$ ($C_{BG} = \varepsilon_{hBN}/d_b$) is the capacitance per unit area of the top (bottom) graphite gate. The thickness of the hBN flake separating the top (bottom) graphite gate from the twisted multilayer is respectively $d_t = 47$ nm ($d_b = 99$ nm). As in Section S2, we estimate the charge carrier density and displacement field offsets to be D_0/ε_0 ~0.02 V/nm and n_0 ~ 2×10^{11} cm^{-2} respectively.

We first characterize Device 2 by driving a current between Contact 1 and Contact 6 [Fig. S6(b)] and measuring the local four-probe resistance, $R_L = R_{xx}$, between Contact 4 and Contact 5 as a function of n and D [Fig. S6(c)]. Near n ~ $\pm6.5\times10^{12}$ cm^{-2}, we observe resistance peaks from moiré band insulator states corresponding to a twist angle of $\theta_M = 1.67°\pm0.05°$. Their dependence on the displacement field points to the origin of the BI being from the moiré between the two middle BLG layers. Namely, applying a small either positive or negative displacement field pushes the charges away from the middle moiré interface. Thus, the middle moiré BI states are effectively shortened by either the topmost or bottommost conductive BLG which results in decreasing R_{xx}.

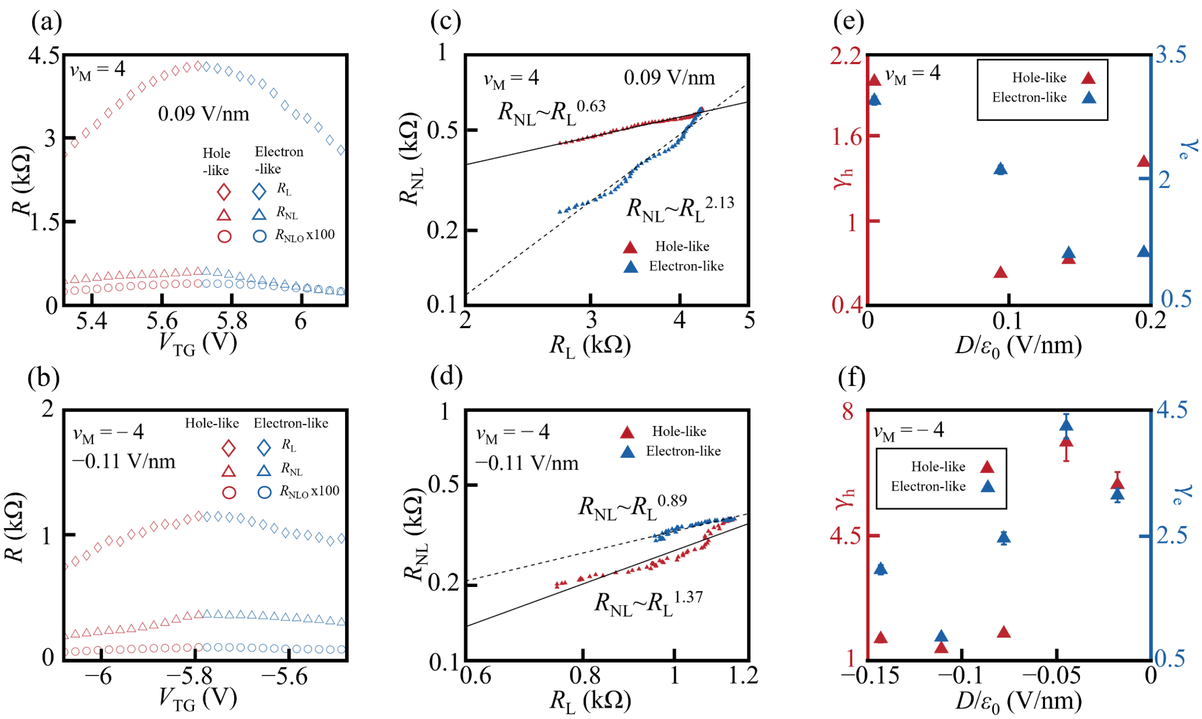

FIG. S7. Valley Hall effect in second device. (a) and (b) The dependance of the local (R_L), nonlocal (R_{NL}) and nonlocal Ohmic resistances (R_{NLO}) on the top graphite gate voltage (V_{TG}) near $\nu_M = 4$ and $\nu_M = -4$ BI states at $D/\varepsilon_0 = 0.09$ V/nm and $D/\varepsilon_0 = -0.11$ V/nm correspondingly. The color indicates the types of carriers involved in electrical transport. (c) and (d) R_{NL} as a function of R_L for hole-like (red) and electron-like (blue) carriers near $\nu_M = \pm4$ and the displacement fields as in (a) and (b). For each carrier type, the solid and dashed lines are power law fits R_{NL}~R_L^{γ}. (e) and (f) The fitted curve exponents $\gamma = \gamma_h$ (γ_e) for the hole- (electron-) like carriers as a function of displacement field near $\nu_M = \pm4$.

At middle moiré fillings of $\nu_M = \pm4$ in Device 2, we observe a substantial nonlocal resistance $R_{NL} = V_{48}/I_{57}$ [Fig. S6(d)], when a current is driven from Contact 5 to Contact 7, and the voltage is measured between Contact 4 and Contact 8. The measured nonlocal resistance at $\nu_M = \pm4$ is more than two orders of magnitude larger [Figs. S7(a) and S7(b)], than the expected contribution from nonlocal Ohmic currents $R_{NLO} = R_L(w/L)\exp(-L/\lambda)$, where $\lambda = w/\pi$; $w = 0.8$ µm, $L = 1.6$ µm are the width and length of the channel. Therefore, the measured nonlocal signal cannot be due to stray Ohmic currents and should come from a Berry curvature hot spot. To confirm this, we study the dependence of R_{NL} on R_L near the BI peak for electron-(Fig. S7, blue), and hole-like (Fig. S7, red) carriers controlled by the graphite top gate voltage. For a selected carrier type (either hole- or electron-like) near the $\nu_M = \pm 4$ BI states, the log-log plots [Figs. S7(c) and S7(d)] of R_{NL} as a function of R_L exhibit a clear power law dependence fitted by a trendline $R_{NL} \sim R_L^{\gamma}$. For the fitted curves plotted as solid (dashed) lines in Figs. S7(c) and S7(d) corresponding to the hole-(electron-like) carriers, we extract the exponents $\gamma_h(\gamma_e)$ whose values indicate the strength of the valley Hall effect. The latter can be tuned by applied out-of-plane displacement field [Figs. S7(e) and S7(f)]. Near $\nu_M = 4(-4)$, both carrier type exponents exhibit a trend of having the lowest values near $D_0/\varepsilon_0 \sim 0.1(-0.1)$ V/nm, being a signature of γ decreasing toward zero due to saturation of valley conducting channel. Specifically, for hole-like carriers near $\nu_M = 4$ at $D_0/\varepsilon_0 \sim 0.09$ V/nm, the exponent of the scaling relation $R_{NL} \sim R_L^{\gamma}$ reaches $\gamma_h = 0.63$ suggesting a significant reinforcement of the Berry curvature hot spot. This can potentially be explained by two competing inter-moiré interactions between the middle and topmost moiré interfaces and between the middle and bottommost moirés. At $|D_0/\varepsilon_0| < 0.1$ V/nm, both the topmost and the bottommost moirés are depleted of charge carriers thus equally affecting the middle moiré interface and resulting in further amplification of the valley currents.

References:

[1] Y. Saito, J. Ge, K. Watanabe, T. Taniguchi, and A. F. Young, Independent superconductors and correlated insulators in twisted bilayer graphene, Nat. Phys. **16**, 926 (2020).

[2] C. R. Dean, A. F. Young, I. Meric, C. Lee, L. Wang, S. Sorgenfrei, K. Watanabe, T. Taniguchi, P. Kim, K. L. Shepard, et al., Boron nitride substrates for high-quality graphene electronics, Nature Nanotech **5**, 10 (2010).

[3] L. Wang, I. Meric, P. Y. Huang, Q. Gao, Y. Gao, H. Tran, T. Taniguchi, K. Watanabe, L. M. Campos, D. A. Muller, et al., One-Dimensional Electrical Contact to a Two-Dimensional Material, Science **342**, 614 (2013).

[4] Z. Zhu, S. Carr, D. Massatt, M. Luskin, and E. Kaxiras, Twisted Trilayer Graphene: A Precisely Tunable Platform for Correlated Electrons, Phys. Rev. Lett. **125**, 116404 (2020).

[5] M. Koshino, Band structure and topological properties of twisted double bilayer graphene, Phys. Rev. B **99**, 235406 (2019).

[6] Y. Shimazaki, M. Yamamoto, I. V. Borzenets, K. Watanabe, T. Taniguchi, and S. Tarucha, Generation and detection of pure valley current by electrically induced Berry curvature in bilayer graphene, Nature Phys **11**, 1032 (2015).

[7] M. Sui, G. Chen, L. Ma, W.-Y. Shan, D. Tian, K. Watanabe, T. Taniguchi, X. Jin, W. Yao, D. Xiao, et al., Gate-tunable topological valley transport in bilayer graphene, Nature Phys **11**, 1027 (2015).

[8] S. Sinha, P. C. Adak, R. S. Surya Kanthi, B. L. Chittari, L. D. V. Sangani, K. Watanabe, T. Taniguchi, J. Jung, and M. M. Deshmukh, Bulk valley transport and Berry curvature spreading at the edge of flat bands, Nat Commun **11**, 5548 (2020).

[9] R. V. Gorbachev, J. C. W. Song, G. L. Yu, A. V. Kretinin, F. Withers, Y. Cao, A. Mishchenko, I. V. Grigorieva, K. S. Novoselov, L. S. Levitov, et al., Detecting topological currents in graphene superlattices, Science **346**, 448 (2014).

[10] Y. Li, M. Amado, T. Hyart, G. P. Mazur, and J. W. A. Robinson, Topological valley currents via ballistic edge modes in graphene superlattices near the primary Dirac point, Commun

Phys **3**, 1 (2020).
[11] C. Ma, Q. Wang, S. Mills, X. Chen, B. Deng, S. Yuan, C. Li, K. Watanabe, T. Taniguchi, X. Du, et al., Moiré Band Topology in Twisted Bilayer Graphene, Nano Lett. **20**, 6076 (2020).
[12] Z. Wu, B. T. Zhou, X. Cai, P. Cheung, G.-B. Liu, M. Huang, J. Lin, T. Han, L. An, Y. Wang, et al., Intrinsic valley Hall transport in atomically thin MoS2, Nat Commun **10**, 611 (2019).